High Confinement Mode and Edge Localized Mode Characteristics in a Near-Unity Aspect Ratio Tokamak

K. E. Thome,[*] M. W. Bongard, J. L. Barr, G. M. Bodner, M. G. Burke, R. J. Fonck,
D. M. Kriete, J. M. Perry, and D. J. Schlossberg

Department of Engineering Physics, University of Wisconsin-Madison, 1500 Engineering Drive, Madison, Wisconsin 53706, USA

Tokamak experiments at near-unity aspect ratio $A \lesssim 1.2$ offer new insights into the self-organized H-mode plasma confinement regime. In contrast to conventional $A \sim 3$ plasmas, the L-H power threshold P_{LH} is $\sim 15\times$ higher than scaling predictions, and it is insensitive to magnetic topology, consistent with modeling. Edge localized mode (ELM) instabilities shift to lower toroidal mode numbers as A decreases. These ultralow-A operations enable heretofore inaccessible $J_{\text{edge}}(R, t)$ measurements through an ELM that show a complex multimodal collapse and the ejection of a current-carrying filament.

Future fusion plasma systems based on the tokamak magnetic confinement concept, including ITER, are almost uniformly assumed to operate in the high confinement (H-mode) regime due to its superior performance compared to the low confinement (L-mode) regime [1,2]. These plasmas have improved energy and particle confinement, reduced turbulence and cross-field transport, and steep edge gradients compared to L-mode plasmas. The equilibrium and stability properties of the H-mode state have been extensively documented since its discovery [3], but much of its physical understanding remains empirical.

Elucidating the underlying physics of this complex, self-organizing regime is interesting in its own right, but it is also critical to future projections of plasma performance and ultimately the viability of a fusion reactor. In particular, a deeper understanding of the L-H transition threshold power P_{LH} [4,5] and edge localized mode (ELM) [6,7] instability behavior is required.

The H-mode is spontaneously accessed when a power greater than P_{LH} is applied to an L-mode plasma. Work to develop and experimentally validate models of the L-H transition dynamics is ongoing [8–10], but no standard model is yet available. Thus, P_{LH} is currently best described by empirical scalings that provide some insight into the threshold behavior but are limited in their applicability.

The strong edge gradients in the H-mode excite ELMs, which relax these gradients by ejecting possibly damaging levels of energy and particles onto the confining walls. Some ELM onset is explained by the peeling-ballooning model [11], but nonlinear treatments are needed for power deposition projections in next-step devices [12–14].

Validation of H-mode models and ELM mitigation techniques benefits from contributions at different experimental parameters in the H-mode confinement regime. Specifically, varying the toroidal aspect ratio A affects aspects of H-mode access, equilibrium, and stability [15]. Spherical tokamaks (STs, $A < 2$) and conventional advanced tokamaks

(ATs, $A \sim 3 - 4$) have comparable H-mode energy confinement [16] and access to empirically categorized ELM types [7,17–19]. In contrast, details of P_{LH} [4,5,20,21] and ELM characteristics [17,18,22] differ. In particular, the lower toroidal field B_T of STs results in an increased peeling drive [23,24], which modifies the ELM stability space.

Insights into characterizing both the H-mode and ELMs can be obtained from high-toroidicity tokamak experiments at a near-unity aspect ratio, $A \lesssim 1.2$. The low required toroidal field ($B_T < 1$ T) for stable plasmas in STs allows ready access to the H-mode, with only Ohmic heating, since $P_{LH} \propto B_T^{0.8}$ [5]. Operation at $A \lesssim 1.2$ and $B_T \sim 0.15$ T produces H-mode conditions with low temperatures, allowing direct pedestal diagnostic access via probes with high spatiotemporal resolution.

This Letter reports the first observations of H-mode properties at a near-unity aspect ratio. As $A \to 1$, differences in H-mode properties are found with respect to P_{LH}, ELM magnetic structures, and magnetic configuration effects. Conditions for H-mode access in Ohmically heated plasmas, H-mode signatures, direct measurement of edge pressure and current pedestals, estimates of the energy confinement, P_{LH} behavior, and ELM magnetic structures are reported. The first detailed edge current profile measurements spanning an ELM event on Alfvénic time scales ($t < 200 \ \mu$s) are also presented.

These experiments were performed on the ultralow aspect ratio Pegasus Toroidal Experiment [25]. It is a mid-sized spherical tokamak with $I_p \sim 0.15$ MA using Ohmic heating, major radius $R_0 \sim 0.35$ m, minor radius $a \sim 0.30$ m, $A \equiv R_0/a \lesssim 1.2$, elongation $\kappa = 1$–3, triangularity $\delta = 0.3$–0.6, $B_T \sim 0.15$ T, $\Delta t_{\text{pulse}} \sim 25$ ms, and limited and diverted magnetic topologies.

The H-mode regime is routinely accessed at $A \lesssim 1.2$ using only Ohmic heating. Similar to other STs, the L-H transition is facilitated and/or improved through the use of high-field-side (HFS) fueling [26]. The

H-mode is accessible in both limited and diverted magnetic configurations.

Figure 1 compares signals from limited L-mode and H-mode plasmas at $A \lesssim 1.2$. Figures 1(a)–1(c) show waveforms from L- and H-mode discharges with comparable $I_p \sim 0.1$ MA [Fig. 1(a)]. They differed only by fueling method, with the L-mode plasma exclusively fueled from the low-field-side (LFS) and the H-mode from the HFS. The plasmas had comparable density ($\bar{n}_e \sim 1 \times 10^{19}$ m^{-3}) and shape ($A \approx 1.22$, $\kappa \approx 2.4$, $\delta \approx 0.57$) at the L-H transition time. This transition is indicated in Fig. 1(b) when D_α emissions drop and in Fig. 1(c) by the diamagnetic loop toroidal flux Φ_D diverging from $\Phi_D \sim 1$ mWb (L-mode) to $\Phi_D \geq 2$ mWb (H-mode). A prominent spike in the H-mode D_α signal accompanies a large (type I) ELM. Magnetic equilibrium reconstructions show that the increase in paramagnetism [Fig. 1(c)] in the H-mode includes changes in both stored energy W_K and internal inductance l_i. In these low-A discharges, the paramagnetic contribution from increased l_i dominates the decreases in Φ_D due to the higher W_K.

Fast camera images of similar plasmas are shown in Figs. 1(d) and 1(e). An L-mode plasma with a bright, turbulent edge is shown in Fig. 1(d). In contrast, a sharp, quiescent, and dim edge of an H-mode plasma between ELMs is shown in Fig. 1(e). A contrast-enhanced image of an ELM [Fig. 1(f)] shows 3D field-aligned filaments accompanying the ELM burst, similar to MAST observations [27].
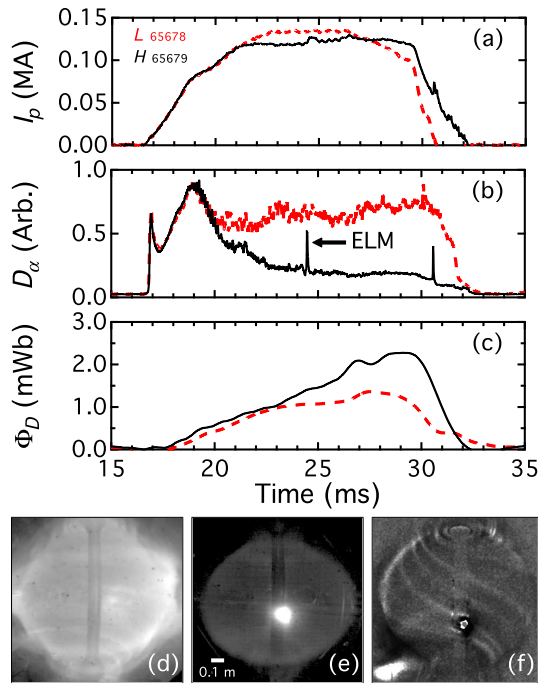
The edge current profile J_{edge} was measured using a 16-channel array of shielded Hall effect sensors inserted into the edge plasma at $Z = 0$ cm [28]. The sensors directly measure the internal $B_Z(R,t)$. The $J_\phi(R,t)$ profile is then derived from a smoothed spline fit of these measurements [23,29]. As such, the derived current is a lower limit estimate of the total $J_\parallel(R,t)$.

Current and pressure pedestals form in H-mode plasmas between ELMs. The $B_Z(R)$ and $J_{\text{edge}}(R)$ profiles for the discharges of Figs. 1(a)–1(c) at 28 ms are shown in Figs. 2(a) and 2(b). The H-phase pedestal width is about 2 cm, contracting from approximately double that in the L-phase. The net H-mode increase in edge current arises both from the formation of the H-mode pedestal and the redistribution of current as l_i increases. At this very low A, $J_\phi(R)$ is very strongly peaked on the HFS at $l_i \sim 0.3$ (L-mode) and more uniformly distributed in radius at $l_i \gtrsim 0.4$ (H-mode).

Initial measurements of an H-mode electron pressure pedestal [Fig. 2(c)] were obtained from multishot radial scans of an insertable triple Langmuir probe. Displacement of the plasma edge from internal $n = 1$ tearing mode activity was accounted for by conditionally sampling the pressure profile at its high and low phases. The two radially offset profiles were then combined for each discharge type by shifting them with respect to R_{edge} and removing their dc offsets. The L-mode profile is best fit bilinearly, whereas the H-mode profile is best fit using a modified hyperbolic
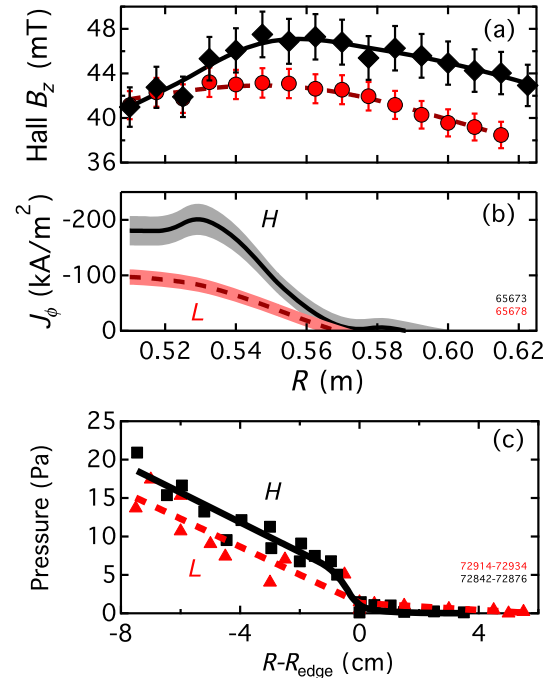

FIG. 1. I_p (a), D_α signal (b), and Φ_D (c) of H-mode (solid black line) and L-mode (dashed red line) discharges. Visible images ($\Delta t \sim 10$ μs) of limited L-mode (d) and H-mode (e) plasmas and a contrast-enhanced ELM (f).

FIG. 2. Pedestal formation in the H-mode. Measured $B_Z(R)$ (a) and inferred $J_\phi(R)$ (b) in lab space for H-mode (solid line, diamonds) and L-mode (dashed line, circles) plasmas. (c) Multishot pressure profile constructed from L-mode (triangle) and H-mode (square) discharges.

tangent profile [30]. These data suggest an H-mode electron pressure pedestal scale length of about 1 cm.

The energy confinement time τ_e was measured for limited and diverted L- and H-mode discharges using time-evolving magnetic reconstructions of the plasma stored energy during the I_p flattop, including corrections for the changing total (kinetic and magnetic) plasma energies $dW/dt = dW_K/dt + dW_M/dt$. Radiated power was previously estimated to be negligible [31].

The energy confinement time ranges from 1 to 7 ms for these discharges. Since the properties of the plasmas differed, τ_e is best described by normalization to the $IPB98(y, 2)$ empirical H-mode scaling [2] with the H_{98} factor, where $H_{98} \equiv \tau_e/\tau_{e,IPB98(y,2)}$. The average H_{98} factor for the L-mode is 0.5 ± 0.2 and for the H-mode is 1.0 ± 0.2. H-mode discharges at $A \lesssim 1.2$ show a confinement improvement of at least approximately double that of L-mode plasmas, similar to other tokamaks [1]. Passive ion spectroscopy and preliminary Thomson scattering measurements of H-mode plasmas qualitatively suggest increased ion and electron temperatures compared to L-mode plasmas.

The confinement improvement in the H-mode is comparable in limited and diverted plasmas. Since the discharges have τ_e evolving throughout their relatively short pulse, more precise comparisons of these regimes will be possible when longer discharge pulses become available.

The L-H power threshold was measured as a function of input power, density, and magnetic topology. These experiments varied the Ohmic input power $P_{OH} = I_p V_{loop}$ in the range of 0.05 to 0.6 MW, $\bar{n}_e = 0.5 - 5 \times 10^{19}$ m^{-3} (Greenwald fraction $\bar{n}_e/n_G \approx 0.1$–0.8 [32]), and in inner-wall limited and favorable single null diverted magnetic configurations with a typical inner-wall gap at the midplane of about 1–3 cm. Figure 3 shows the power required to access the H-mode as a function of $\bar{n}_e$. P_{OH} is normalized to the empirical ITPA08 P_{LH} scaling B_T and surface area S dependencies [5]. In most cases, the plasma shape was
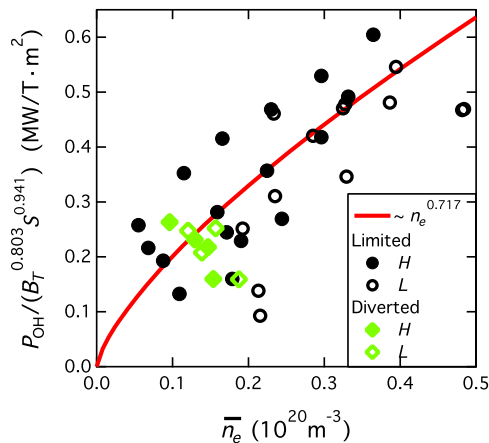
estimated using a multifilament fast boundary reconstruction code coupled to a wall current filament model and constrained by external magnetic measurements. The power threshold is given by $P_{LH} = P_{OH} - dW/dt$ at the L-H transition time. Magnetic reconstructions of a subset of discharges in Fig. 3 show that the dW/dt correction is about 30% of P_{OH} in these experiments.

While this simplified analysis and shot-to-shot variation result in some scatter, there is a general separation of the L and H data, indicating the location of the power threshold. This threshold increases with density in a fashion consistent with the ITPA empirical scaling. However, the magnitude of the scaling underpredicts the measured P_{LH} by $\sim 15 \times$. Unlike some high-A tokamaks [33] no apparent minimum in $P_{LH}(\bar{n}_e)$ is observed in Pegasus. The operating space for limited and diverted plasma topologies overlaps: $P_{LH}^{LIM} \approx P_{LH}^{DIV}$. This result is in contrast to higher-A devices where $P_{LH}^{LIM} \geq (1.5 - 3)P_{LH}^{DIV}$ for favorable single null diverted plasmas [34,35].

The power threshold on Pegasus exceeds predictions from accepted scalings by an order of magnitude or more. Figure 4 shows P_{LH} for Pegasus and several tokamaks in the ITPA database [5] normalized to the ITPA08 scaling. This scaling was derived from experiments with $A \sim 2.5$–5. As $A \to 1$, P_{LH}/P_{ITPA08} significantly increases, confirming a trend suggested by NSTX [5,20] and MAST [4,5]. Theoretical models to explain these variations with A are not yet available.

Nevertheless, some of the unique characteristics of P_{LH} at near-unity A are consistent with the FM^3 L-H transition model [8]. This model postulates that the P_{LH}-minimizing density n_e^{min} is related to a critical edge collisionality. For Pegasus, FM^3 predicts $n_e^{min} \sim 1 \times 10^{18}$ m^{-3} ($\bar{n}_e \ll 0.1 n_G$). This is not accessible in Ohmic plasmas, consistent with the absence of n_e^{min} in Fig. 3. The difference in limited and diverted power thresholds is posited to be due to the safety factor $q_\star$ at the radial location of the L-H transition, which FM^3 defines to be within a pressure gradient scale length of the last closed flux surface. In practice, this location is in the outer few percent of the normalized poloidal flux. At high A, $q_\star^{LIM} < q_\star^{DIV}$, while the increased edge shear at low

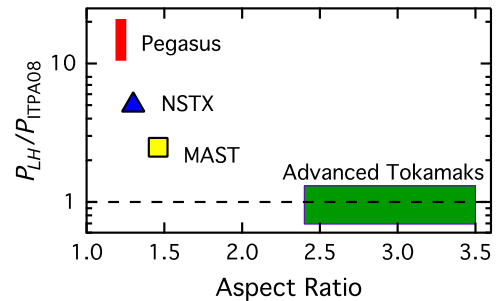FIG. 3. P_{OH} normalized by B_T and S ITPA dependencies vs density.

FIG. 4. Measured P_{LH} compared to the ITPA scaling for several tokamaks at different aspect ratios.

A results in $q_\star^{\mathrm{LIM}} \approx q_\star^{\mathrm{DIV}}$. FM³ asserts that $P_{LH}^{\mathrm{LIM}}/P_{LH}^{\mathrm{DIV}} \approx (q_\star^{\mathrm{LIM}}/q_\star^{\mathrm{DIV}})^{-7/9}$. Thus, the observations that $P_{LH}^{\mathrm{LIM}} \sim P_{LH}^{\mathrm{DIV}}$ at low A and $P_{LH}^{\mathrm{LIM}} > P_{LH}^{\mathrm{DIV}}$ at high A are in agreement with this model. The P_{LH} magnitude at low A is not consistent with FM³ since it explicitly replicates the ITPA08 scaling.

Two classes of ELMs have been observed in Pegasus H-mode plasmas. Classification of ELMs by their frequency-power relationship is not possible due to the lack of auxiliary heating. Nonetheless, they are identified here by their toroidal mode number n spectrum and their occurrence at different values of P_{OH}/P_{LH}. Small, type III-like ELMs are present at $P_{\mathrm{OH}} \sim P_{LH}$. As P_{OH} is increased, they transition to large, type I-like ELMs. Large ELM virulence increases further as P_{OH} increases, often terminating discharges when $P_{\mathrm{OH}}/P_{LH} \gtrsim 2$.

Mode spectra are derived from cross-phase analysis of near-edge Mirnov coil array measurements [24]. Multiple n modes are observed during both ELM types, consistent with the simultaneous presence of multiple unstable peeling-ballooning modes. Figure 5 shows the magnetic fluctuation autopower spectrum of a single probe and the toroidal mode number of discrete modes sampled over the duration of single ELM events. Type III ELMs have $n \le 4$ [Fig. 5(a)]. Type I ELMs have intermediate $5 < n < 15$ [Fig. 5(b)] present. This trend in n spectra is similar to that reported at $A \sim 1.3$ in NSTX [17].

When comparing dominant n spectra in type I and type III ELMs, a marked difference is found between low- and high-A plasmas. At high A, type III spectra are dominated by mode numbers greater than those seen in type I ELMs ($n_{\mathrm{III}} > n_{\mathrm{I}}$) [19,22]. However, at low A, type III spectra are dominated by mode numbers less than those in the corresponding type I ELMs ($n_{\mathrm{III}} < n_{\mathrm{I}}$). At both aspect ratios, type I ELM spectra are generally dominated by intermediate $n \sim 6–15$, but at low A (Pegasus and NSTX [17]), the mode numbers are somewhat lower than at high A. These trends presumably reflect the increased peeling mode drive ($\propto J_{\mathrm{edge}}/B_T$) [36,37] that naturally occurs at low A. This influence of the peeling drive on ELM n spectra is also reflected in lowered dominant n values with increased J_{edge} at high A [38].

Both ELM types generate edge "current-hole" perturbations. Type I ELMs can expel current-carrying filaments. These features are hypothesized by electromagnetic blob
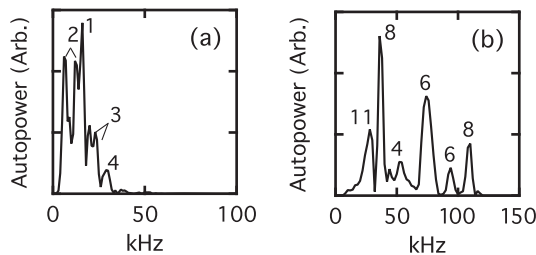
transport theory [39], observed in nonlinear ELM simulation [40], and are qualitatively similar to those observed in earlier peeling mode studies on Pegasus [23].

Measurements of the edge current density profile in Pegasus provide the first experimental evidence of its complex spatiotemporal evolution during an ELM event. Figure 6 shows $J_{\mathrm{edge}}(R, t)$ across the pedestal spanning a type I ELM crash. Time values are referenced to the first detectable rise in ELM magnetic activity [Fig. 6(a)]. The pre-ELM current pedestal builds over Figs. 6(b)–6(d). During the following collapse phase [Figs. 6(e)–6(j)], J_{edge} first develops fragmentary "current-hole" perturbations [Fig. 6(f)] that expand past the equilibrium last closed flux surface location at $R \approx 0.56$ m [Fig. 6(g)]. Current is transported radially outward [Figs. 6(h)–6(i)]. J_ϕ then coalesces into two regions separated at $R \approx 0.57$ m that become the post-ELM pedestal and a current-carrying filament [Fig. 6(j)]. The filament is subsequently expelled and radially accelerates away from the plasma. An outwardly propagating filament is also observed on the fast visible imaging at the Hall sensor locations at this time.

Demonstration of H-mode access in a relatively small confinement experiment with modest plasma parameters opens new opportunities to test our understanding of this important and interesting phenomenon. This Letter extends observations of the H-mode regime to near-unity $A \lesssim 1.2$. Notably, the L-H power threshold and ELM magnetic structure exhibit strong A dependencies. P_{LH} in limited and

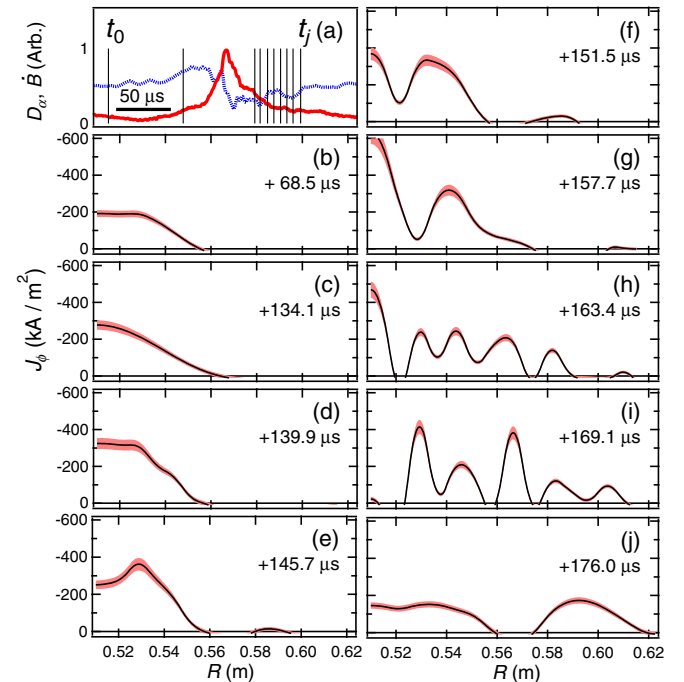FIG. 5. Magnetic fluctuation autopower spectra and toroidal mode numbers of small (a) and large (b) ELMs.

FIG. 6. Current profile evolution through large ELM. (a) D_α (solid red line) and $\dot{B}$ (dashed blue line) versus time, profile time indicators (thin black lines); (b)–(j) edge $J_\phi(R, t)$ at specified $t - t_0$ values.

diverted plasmas is equivalent on Pegasus. This is in contrast to high-A experiments, where the diverted threshold is much lower. P_{LH} increasingly disagrees with high-A scaling predictions as $A \rightarrow 1$. ELM magnetic structures are uniformly lower n than at $A \sim 3$. A complex, multimodal $J_{\text{edge}}(R, t)$ evolution through an ELM event leads to an average current hole at the edge and consequent filament ejection. These and future measurements should provide rich opportunities to test models of the L-H transition and nonlinear simulations of ELMs in high-performance fusion plasmas.

Data from this publication are publicly available in openly documented, machine-readable formats [41].

---

*Corresponding author.
thomek@fusion.gat.com

[1] F. Wagner, Plasma Phys. Controlled Fusion **49**, B1 (2007).
[2] ITER Physics Basis Editors, Nucl. Fusion **39**, 2175 (1999).
[3] F. Wagner et al., Phys. Rev. Lett. **49**, 1408 (1982).
[4] T. Takizuka and the ITPA H-Mode Database Working Group, Plasma Phys. Controlled Fusion **46**, A227 (2004).
[5] Y. R. Martin, T. Takizuka, and the ITPA CDBM H-mode Threshold Data Group, J. Phys. Conf. Ser. **123**, 012033 (2008).
[6] P. T. Lang et al., Nucl. Fusion **53**, 043004 (2013).
[7] A. W. Leonard, Phys. Plasmas **21**, 090501 (2014).
[8] W. Fundamenski, F. Militello, D. Moulton, and D. C. McDonald, Nucl. Fusion **52**, 062003 (2012).
[9] J. W. Connor and H. R. Wilson, Plasma Phys. Controlled Fusion **42**, R1 (2000).
[10] Z. Yan, G. R. McKee, R. Fonck, P. Gohil, R. J. Groebner, and T. H. Osborne, Phys. Rev. Lett. **112**, 125002 (2014).
[11] P. B. Snyder et al., Nucl. Fusion **49**, 085035 (2009).
[12] G. T. A. Huijsmans and A. Loarte, J. Nucl. Mater. **438**, S57 (2013).
[13] C. F. Maggi, Nucl. Fusion **50**, 066001 (2010).
[14] G. T. A. Huijsmans, C. S. Chang, N. Ferraro, L. Sugiyama, F. Waelbroeck, X. Q. Xu, A. Loarte, and S. Futatani, Phys. Plasmas **22**, 021805 (2015).
[15] Y. K. M. Peng and D. J. Strickler, Nucl. Fusion **26**, 769 (1986).
[16] M. Valovič, R. Akers, G. Cunningham, L. Garzotti, B. Lloyd, D. Muir, A. Patel, D. Taylor, M. Turnyanskiy, and M. Walsh, Nucl. Fusion **49**, 075016 (2009).
[17] R. Maingi et al., Nucl. Fusion **45**, 1066 (2005).
[18] H. Meyer et al., Nucl. Fusion **49**, 104017 (2009).
[19] H. Zohm, Plasma Phys. Controlled Fusion **38**, 105 (1996).
[20] R. Maingi et al., Nucl. Fusion **50**, 064010 (2010).
[21] H. Meyer et al., Nucl. Fusion **46**, 64 (2006).
[22] T. Kass, S. Günter, M. Maraschek, W. Suttrop, H. Zohm, and ASDEX Upgrade Team, Nucl. Fusion **38**, 111 (1998).
[23] M. W. Bongard, R. J. Fonck, C. C. Hegna, A. J. Redd, and D. J. Schlossberg, Phys. Rev. Lett. **107**, 035003 (2011).
[24] M. W. Bongard, K. E. Thome, J. L. Barr, M. G. Burke, R. J. Fonck, E. T. Hinson, A. J. Redd, and D. J. Schlossberg, Nucl. Fusion **54**, 114008 (2014).
[25] G. D. Garstka et al., Nucl. Fusion **46**, S603 (2006).
[26] A. R. Field et al., Plasma Phys. Controlled Fusion **46**, 981 (2004).
[27] A. Kirk, B. Koch, R. Scannell, H. R. Wilson, G. Counsell, J. Dowling, A. Herrmann, R. Martin, M. Walsh, and the MAST Team, Phys. Rev. Lett. **96**, 185001 (2006).
[28] M. W. Bongard, R. J. Fonck, B. T. Lewicki, and A. J. Redd, Rev. Sci. Instrum. **81**, 10E105 (2010).
[29] C. C. Petty, W. R. Fox, T. C. Luce, M. A. Makowski, and T. Suzuki, Nucl. Fusion **42**, 1124 (2002).
[30] R. J. Groebner and T. N. Carlstrom, Plasma Phys. Controlled Fusion **40**, 673 (1998).
[31] K. E. Thome, J. L. Barr, M. W. Bongard, M. G. Burke, A. S. Dowd, R. J. Fonck, E. T. Hinson, A. J. Redd, and D. J. Schlossberg, Bull. Am. Phys. Soc. **56**, 244 (2011).
[32] M. Greenwald, J. L. Terry, S. M. Wolfe, S. Ejima, M. G. Bell, S. M. Kaye, and G. H. Neilson, Nucl. Fusion **28**, 2199 (1988).
[33] Y. Ma, J. W. Hughes, A. E. Hubbard, B. LaBombard, R. M. Churchill, T. Golfinopolous, N. Tsujii, and E. S. Marmar, Nucl. Fusion **52**, 023010 (2012).
[34] K. H. Burrell et al., Plasma Phys. Controlled Fusion **31**, 1649 (1989).
[35] T. N. Carlstrom, M. Shimada, K. H. Burrell, J. DeBoo, P. Gohil, R. Groebner, C. Hsieh, H. Matsumoto, and P. Trost, in Proceedings of the 16th European Conference on Controlled Fusion and Plasma Physics (Europhysics Conference Abstracts, Venice, 1989), p. 241.
[36] R. Maingi et al., Phys. Rev. Lett. **103**, 075001 (2009).
[37] J. W. Connor, Plasma Phys. Controlled Fusion **40**, 531 (1998).
[38] C. P. Perez et al., Nucl. Fusion **44**, 609 (2004).
[39] J. R. Myra, Phys. Plasmas **14**, 102314 (2007).
[40] S. J. P. Pamela, G. T. A. Huysmans, M. N. A. Beurskens, S. Devaux, T. Eich, S. Benkadda, and JET EFDA Contributors, Plasma Phys. Controlled Fusion **53**, 054014 (2011).
[41] K. E. Thome, M. W. Bongard, J. L. Barr, G. M. Bodner, M. G. Burke, R. J. Fonck, D. M. Kriete, J. M. Perry, and D. J. Schlossberg, https://dx.doi.org/10.18138/1209110.